Supporting Information

Min et al. 10.1073/pnas.1120218109

SI Text

SI Materials and Methods. ***Microbiology.*** *Escherichia coli* cells [strain RP437, wild type for chemotaxis(1)] were collected from a single colony on an agar plate and grown overnight in 1 ml tryptone broth [1% (wt/vol) Bacto tryptone and 0.8% (wt/vol) NaCl] (2). The overnight culture was diluted 100-fold into 1 ml tryptone broth and grown for 4.5 h to mid-log phase ($OD_{600} \approx 0.5$). Cells were grown at 30 °C with 265 rpm rotation in 15-mL round bottom Falcon tubes. The final culture was diluted 10-fold into "trap motility buffer" (TMB). TMB contained 70 mM NaCl, 0.1 mM methionine, 100 mM Tris-Cl, 2% (wt/vol) glucose, and an oxygen-scavenging system (80 $\mu g\,ml^{-1}$ glucose oxidase and 13 $\mu g\,ml^{-1}$ catalase; EMD Chemicals 345386 and 219001, respectively) to reduce oxidative damage to the cells by the infrared trapping light (3, 4). The oxygen-scavenging system was added immediately before the beginning of the experiment. Under anaerobic conditions, trapped cells grew and divided at the expected rate, and exhibited run and tumble durations within the range reported in the literature (4). We performed control chemotaxis experiments using a 2-D swimming assay, following the protocol from Alon et al. (5). We observed similar adaptation times with (160 ± 30 s) and without (200 ± 30 s) the oxygen-scavenging system in the medium. Methionine provides the methyl groups necessary for chemotactic adaptation to occur (6). Glucose acts as a substrate for the oxygen-scavenging system and provides energy for cell swimming under anaerobic condition (7). Various concentrations of L-aspartate (1–1,000 mM) were added as a chemical stimulus.

Optical trap setup. A detailed description of the optical tweezers design can be found elsewhere (4, 8). Briefly, the optical tweezers component consisted of two orthogonally polarized beams from a single 5-W, 1,064-nm diode-pumped solid-state laser (YLR-5-1064-LP; IPG Photonics). Both beams were tightly focused to generate optical traps by a 60 ×, water-immersion (1.2 numerical aperture) microscope objective (Nikon). The separation between the two traps was controlled by a piezo-actuated mirror stage (Nano-MTA; Mad City Labs). An identical objective lens collected transmitted light for position detection and bright-field imaging. The flow chamber was positioned between the two objective lenses and was displaced relative to the two traps in all directions by a motorized three-axis translational stage (ESP300; Newport). Cell motion was detected directly by the optical traps themselves, using back-focal plane interferometry, in which trap light scattered by an object relays the object's position relative to the trap in all three directions (9). Epifluorescence excitation in widefield configuration was provided by a 30-mW, 532-nm diode laser (TECGL-30; World Star Tech) to excite rhodamine B for gradient calibration. Emitted fluorescence light passed through a dichroic mirror (Di01-R532-25 × 36, single-edge 532-nm laser dichroic; Semrock) and an emission filter (HQ600/100 m-2p, band-pass 550–650 nm; Chroma) before being imaged onto an intensified charge-coupled device (I-PENTAMAX; Princeton Instruments).

Fluidics. Glass coverslips (Fisher 12-545-M, 24 × 60 − 1) were sonicated in dry acetone for 5 min and rinsed with deionized water. Remaining water was spun off by centrifuging at 1,000 rpm for 3 min. The flow channel pattern was cut out from Nescofilm (Karlan) and placed between two coverslips, one of which had custom-drilled holes (0.05-inch diameter) for inlets and outlets. The Nescofilm flow channel pattern was bonded to coverslips by melting on a hot plate for 4 min. The completed flow chamber was inserted into a custom metal frame where inlet and outlet tubings (Tygon) were screwed on for a tight seal (Fig. S1*A*). The three channels of the flow chamber were continuously injected with appropriate buffers using a syringe pump (PHD2000; Harvard Apparatus) at a linear speed of 70 μm/s. We performed control experiments to test the effect of flow on cell swimming parameters. Individual trapped cells monitored in 70 μm/s flow exhibited an approximately 10% decrease in run duration and an approximately 20% decrease in tumble duration, compared to no-flow conditions. The tumble bias remained relatively constant over the same range of flow rates ($N = 8$ cells). In step-up stimulus experiments, the top channel was injected with TMB, L-aspartate, and rhodamine B. The middle channel contained TMB only, and the bottom channel contained cells in TMB. In step-down stimulus experiments, the top channel contained TMB and rhodamine B, the middle channel contained TMB and L-aspartate, and the bottom channel contained TMB, L-aspartate, and cells. Rhodamine B (Sigma R6626) (100 nM) was used to quantify the gradient profile under the fluorescent illumination of the optical trap setup (Fig. S1 *B* and *C*) prior to each experiment.

Post-processing of the optical trap data. All routines for analyzing optical trap data were written in MATLAB (MathWorks). Raw data obtained at 1,000-Hz sampling frequency were low-pass filtered to 100 Hz, and the amplitude was normalized in non-overlapping 1-s windows (4). Two separate sets of *y*-direction (Fig. 1*A*) signals obtained from the two ends of the cell body were combined by taking the difference for enhancement in signal-to-noise ratio. Using the combined *y*-direction signal, the peak frequency component at each time point was obtained from a continuous wavelet transform. Our wavelet analysis was performed using the complex Morlet mother wavelet in a linearly scaled frequency range of 2–40 Hz. Runs and tumbles were distinguished by applying a single threshold value to the peak frequency time trace. The threshold was determined by examining the distribution of peak frequencies and finding the local minimum between peaks corresponding to run and tumble. For cases in which a clear local minimum could not be found, an arbitrary threshold of 4 Hz was applied. Detected runs and tumbles that were shorter than 100 ms were removed, as our detection limit was expected to be one cycle in the sinusoidal pattern of the running cell (10-Hz body-roll frequency is taken as an arbitrary standard) (4).

Quantifying adaptation features at the population-average level. The run/tumble binary time traces were subsequently analyzed using two different methods. In one method, tumble bias was determined from a 10-s moving window by calculating the fraction of time the cell spent tumbling within the window, and moving the window one data point at a time by 0.01 s (Fig. S2). Because individual tumble bias traces were noisy ($\sigma/\mu = 0.53 \pm 0.16$ at steady-state, $n = 186$ cells), they were averaged across the population (Fig. 2 *A* and *B*). From the population-averaged tumble bias traces, adaptation time and overshoot were quantified by fitting to analytical expressions. For step-up stimuli (Fig. 2*A*), the poststimulus portion of the data was fit to the expression $B(t) = 1/(1 + a\exp(\ln(b)\exp(-c(t - t_{adapt}))))$ using the nonlinear fitting function in MATLAB with a and b as constants and c and t_{adapt} (the adaptation time) as fitting parameters. The constants were defined as $a = (1 - B_\infty)/B_\infty$ and $b = 1 + 1/(1 - B_\infty)$, where B_∞ is the steady-state tumble bias (mean of the last 50 s of data),

which ensured that $B(t) = B_\infty/2$ when $t = t_{adapt}$. This expression is an approximate analytical solution for $B(t)$ following the chemotaxis model of Tu et al. (10) (see *Simulations*) and the approximations outlined in the *SI Text*. Because $B(t)$ above does not have an overshoot feature, we fit the residual using the phenomenological form $R(t) = (\text{data} - B(t))$ to $R(t) = a\,t^b \exp(ct)$, where a, b, and c are fitting parameters. Normalized overshoot amplitude was determined as $(B_{max} - B_\infty)/B_\infty$, where B_{max} is the maximum of $B(t) + R(t)$. For step-down stimuli (Fig. 2*B*), the poststimulus portion of the data was fit with a phenomenological expression $B(t) = B_\infty + a\exp(-t/b) + c\exp(-t/d)$ using the nonlinear fitting function in MATLAB with a, b, c, and d as fitting parameters. From this fit, the adaptation time was $t_{adapt} = \ln b$ and the normalized overshoot amplitude was $(B_{min} - B_\infty)/B_\infty$, where B_{min} is the minimum of $B(t)$.

Quantifying adaptation features at the single-cell level. Alternatively, the run/tumble binary time traces were analyzed in the "event domain" (11). In this method, the run/tumble binary time traces were analyzed by pairing each run with its subsequent tumble (11). For each run/tumble pair event we determined a corresponding tumble bias value [tumble duration / (run duration + tumble duration)] and a duration (run duration + tumble duration) (Fig. S5). Population-averaged event traces (Fig. 3 *A* and *D*) were also constructed event by event, where the tumble bias and duration were averaged across the population for each run/tumble event, enumerated relative to the application of the stimulus. Quantification of abruptness, adaptation time, and overshoot from individual cells was performed in the event domain. For abruptness, we determined the number of "events to adaptation" (ETA) using the Mann–Whitney U test, a nonparametric statistical test for assessing the null hypothesis that two independently obtained samples are equal in magnitude (12). The reference sample consisted of 65 events prestimulus, normalized by the mean of the last 20 events poststimulus to compensate for the possibility of nonexact adaptation. The test sample consisted of a moving five-event window immediately following the application of stimulus. The five-event window was moved one event at a time until adaptation was scored when the U statistic of the test sample approached the expected U within 50% of the standard deviation in U. ETA was the number of events that led to adaptation, and adaptation time was the total duration of the events that led to adaptation. We found that our statistical analysis was more robust when using parameters that increase in response to stimuli and then fall back down as the cell adapts (i.e., run duration for step up, tumble bias for step down). Normalized overshoot amplitude was calculated using the formula (Bias_middle—Bias_after) / Bias_after, where Bias_middle was the mean tumble bias of sixth through 15th events following adaptation as determined above, and Bias_after was the mean tumble bias of the final 20 events poststimulus. ETA, adaptation time, and normalized overshoot amplitude of population-average event traces were determined in the same way as the individual event traces (Fig. S8).

Numerical simulations. Simulating chemotactic adaptation. In order to explore the effect of varying the receptor cluster size and motor switching cooperativity on the abruptness of adaptation (Fig. S10*B*), we performed stochastic simulations to generate a population of run/tumble binary time traces for each parameter condition. All simulations were implemented in MATLAB. We followed closely the model by Tu et al. (10). The kinase activity of CheA, A, was determined as a function of ligand concentration ($[L]$) and methylation level (m) according to $A([L], m) = 1/(1 + \exp(N(f_L([L]) + f_m(m))))$, where N is the receptor cluster size, and $f_L = \ln(1 + [L]/K_{off}) - \ln(1 + [L]/K_{on})$ and $f_m = 2(0.5 - m)$ are the free energy functions that depend only on $[L]$ and m, respectively (10). Free energies were in units of $k_B T$. Note that the value of A ranges from 0 to 1. A can be interpreted as the probability that each CheA is in its active (phosphorylating) state. K_{off} (5 μM) and K_{on} (254 μM) are ligand-binding constants for receptors associated with CheA in inactive and active states, respectively. The values for K_{off} and K_{on} were obtained from fitting the expression for f_L to our adaptation time data (Fig. 2*C*). The exact values of K_{off} and K_{on} affect only the adaptation time and not the abruptness of adaptation. At each time step ($\Delta t = 0.01$ sec, chosen to match the data rate; shorter time steps did not change the results of simulation), the average methylation level of the receptor-CheA complex was adjusted according to $dm/dt = V_R(1 - A) - V_B(A)$ (13). V_R (0.01 s^{-1})and V_B (0.02 s^{-1}) are methylation and demethylation rates, respectively (14). As with K_{off} and K_{on}, the exact values of V_R and V_B only affect the adaptation time. The CheA activity, A, was then converted to the flagellar motor bias, B, via a highly cooperative relation $B(A) = A^H/(A^H + K_A{}^H)$ (15). Note that, as with A, B ranges from 0 to 1. K_A is the value of A at which B is 1/2. Although B is technically a function of CheY-P concentration and not CheA activity, it is commonly assumed that CheY-P concentration and CheA activity are proportional because CheY-P levels equilibrate faster than other processes (16). Because a general model on how the motor bias gets converted to the cell's tumble bias is lacking, we assumed they are proportional. At the first time point, every simulated cell started from the tumble state. At each subsequent time point, the cell had a constant probability of switching to the run state. When the cell was in the run state, on the other hand, its probability of switching to the tumble state depended on the tumble bias. As a result, the average tumble duration did not depend on tumble bias but the average run duration did. This was consistent with a previous study and our own data (17) (Fig. S6). For each combination of N and H values, 100 run/tumble binary time traces were generated. The simulated traces were analyzed in the same way as the experimental data as described above.

Simulating the effect of variations in protein expression level. In order to reproduce the observed population variation in adaptation time (Fig. 3*C*), we simulated a population of cells with stochastic variation in CheR and CheB expression levels. Expression levels of CheR and CheB were varied in a concerted manner because they are expressed from the same operon (18). Simulations were run in the same manner as above, except that values of V_R and V_B were selected from a Gaussian distribution with 10% or 20% standard deviation. We note that this degree of protein number fluctuations is in good agreement with typical values found in the literature (19). This fluctuation level is also close to the theoretical expectation based on the known CheR and CheB average copy numbers in the cell (20), and the assumption that proteins are produced in bursts of 5–10 per mRNA (21, 22). Mean V_R and V_B values were the same as above. One thousand cells were simulated for a given level of variation in CheR and CheB expression and stimulus strength. We analyzed the simulated data traces using the same analysis routine used for experimental data to obtain the adaptation time. The coefficient of variation in adaptation time for the simulated adaptation times and the experimentally measured adaptation times (Fig. 3*C*) are shown in Fig. S4*B*.

Simulating the effect of flagellar motor remodeling. We performed simulations to investigate the effect of flagellar motor remodeling (23) on adaptation kinetics (see *SI Discussion*). Following Yuan et al. (23), we used a modified expression relating the motor CW bias B to CheA activity A: $B(A) = (1 + A/K_A)^{FliM}/((1 + A/K_A)^{FliM} + P(1 + A/(K_A C))^{FliM})$, where FliM is the number of FliM units in the c-ring of the flagellar motor, P is the ratio of the probability that the motor is in the CCW state to the prob-

ability that it is in the CW state in the absence of CheY-P ($A = 0$), and C is the ratio of CheY-P dissociation constants for the CCW and CW states, respectively (23). The time-dependent FliM(t) was modeled according to $\mathrm{dFliM}/dt = V_{\mathrm{on}}(\mathrm{FliM_{max}} - \mathrm{FliM}) - V_{\mathrm{off}}(A)\mathrm{FliM}$. Here, $\mathrm{FliM_{max}}$ (assumed to be 45 in our simulations) is the maximum number of FliM units that can be in the c-ring, and V_{on} (=0.02 s^{-1}) and V_{off} (=0.0194 s^{-1}) are association and dissociation rates of FliM to the c-ring. V_{on} and V_{off} satisfy the steady-state condition $V_{\mathrm{on}}(\mathrm{FliM_{max}} - \mathrm{FliM}_\infty) = V_{\mathrm{off}}(A_\infty)\mathrm{FliM}_\infty$, where A_∞ (=1/3) and FliM_∞ (=34) (14, 23–25) are steady-state CheA activity and number of FliM units, respectively. The flagellar motor remodeling was incorporated in the simulations by varying the value of FliM according to the CheA activity, A, at each time point. The results of these simulations are shown in Fig. S10*D*.

SI Discussion. ***Review of the E. coli chemotaxis network.*** A cell's swimming state is controlled by a cascade of interactions (26, 27) (Fig. S10*A*). Chemical input signals from the environment are sensed by transmembrane receptors that are coupled to the intracellular kinase CheA. Commonly, CheA activity is parametrized by the quantity A, the probability (ranging from 0 to 1) that the kinase is in its active (phosphorylating) state. The activity is a function of the receptor ligand concentration (28); an increase in chemoattractant leads to a decrease in activity and vice versa. In addition to ligand binding, methylation of the receptors also modulates kinase activity; the higher the methylation, the higher the activity. Thus,

$$A = A([L], m), \qquad \textbf{[S1]}$$

where $[L]$ is the ligand concentration and m is the number of methylated receptor sites (ranging from 0 to 8). Notably, A is an increasing function of the methylation m. Receptors are also known to interact and cooperatively modulate CheA kinase activity (16, 29). Ligand binding to one receptor affects the CheA activity in a neighborhood of N interacting receptors (29) (Fig. S10*A*). The net consequence of this interaction is to multiply the effect of methylation m on A by the interacting cluster size N (29, 30).

At the same time, the methylation rate of the receptors is also a function of CheA activity. Methylation and demethylation are controlled by the proteins CheR and CheB, respectively, whose activity depends on A (31). Thus,

$$\frac{dm}{dt} = F(A). \qquad \textbf{[S2]}$$

Though the detailed functional form of $F(A)$ depends on the model used (10, 32), for our purposes it is sufficient to state that $F(A)$ is a decreasing function of A; as CheA activity increases, the rate of methylation decreases. Eqs. **S1** and **S2** describe the negative feedback loop that is responsible for adaptation. As CheA activity is perturbed from its steady-state (by a step up or step down in chemoattractant concentration, for example), this feedback loop ensures its eventual return to the same steady-state (5, 31, 33, 34).

The next link in this chain of interactions is the phosphorylation of the signaling protein CheY by CheA. In its active form, CheY-P binds to the flagellar motors and induces a conformational switch from CCW to CW rotation (17, 35). This interaction is known to be highly cooperative, and described by a sigmoidal function (15) (Fig. S10*A*). At subsaturating conditions, the concentration of CheY-P is proportional to CheA activity, and the CW bias of the motor B (defined as the fraction of time spent in the CW state, a number ranging from 0 to 1) can be written as a Hill function

$$B = \frac{A^H}{A^H + K_A^H}, \qquad \textbf{[S3]}$$

where $H \approx 10$ (depicted in Fig. S10*A*). Importantly, measurements have shown that the steady-state CheA activity sits in the steepest part of this function: $A_\infty = 0.33$, $B_\infty = 0.35$ (where the subscript ∞ denotes the steady-state), and $K_A = 0.35$ (15, 32).

The last component of the cascade of interactions occurs between the flagellar motors and the whole cell. As individual motors that comprise the flagellar bundle undergo a conformational switch from CCW to CW rotation, the cell swimming state switches from a run to a tumble (36). It is important to note that the individual motors in the cell are not perfectly synchronized (37–39), and that the manner in which the collective CCW/CW state of the motors dictates the run/tumble state of the whole cell remains poorly understood (40, 41).

Adaptation abruptness does not reflect the switch-like behavior of the flagellar motor. As discussed in the main text, it is natural to assume that the switch-like manner in which the flagellar rotational state depends on CheY-P level plays a role in abruptness of adaptation. However, we found that this cooperativity, parameterized by the large Hill coefficient ($H \approx 10$) (15), has little to no effect on the abruptness of adaptation (Fig. S9*A*). Instead, we believe the evidence points towards alternate mechanisms further discussed below. The derivation that follows explains this in the context of accepted mathematical model of chemotaxis network.

The strong nonlinearity in the Hill equation Eq. **S3** and the fact that the CheA steady-state level is in the steepest portion of the curve mean that the bias B is only sensitive to changes in A near its steady-state level A_∞. In the context of adaptation, the temporal response in B is almost solely determined by A in its approach to the steady-state. For example, in a chemoattractant step-up experiment, 75% of the amplitude of the adaptation response in bias B (as it increases from 0 to B_∞) comes from the last approximately 15% of the amplitude of the response in A as it approaches A_∞.

To quantify this effect, we consider the temporal response in $B(t)$ and $A(t)$ at a reference time point t_{adapt}, the adaptation time. This was defined in the main text as the time elapsed between the stimulus and when the bias returned to half of its steady-state value. Expanding $A(t)$ in a Taylor series about this time yields

$$A(t_{\mathrm{adapt}}) \approx A_\infty + \left.\frac{dA}{dB}\right|_{B_\infty} (B(t_{\mathrm{adapt}}) - B_\infty) = A_\infty - \left.\frac{dA}{dB}\right|_{B_\infty} \cdot \frac{B_\infty}{2}. \qquad \textbf{[S4]}$$

The second term depends inversely on the slope of the Hill function, dB/dA, which is proportional to H. Using previously determined values (15), the second term is approximately $0.25/H = 0.025 \ll A_\infty$ (i.e., small when H is large). Thus, we may write $A(t) = A_\infty - \Delta A(t)$, valid for times $t \gtrsim t_{\mathrm{adapt}}$, where ΔA is small ($\ll A_\infty$) and proportional to $1/H$.

Based on this observation, we can determine the temporal response of $A(t)$ for $t \gtrsim t_{\mathrm{adapt}}$ (i.e., how A approaches A_∞ in time). Taking Eq. **S2** and Taylor expanding $F(A)$ near the steady-state,

$$\frac{dm}{dt} \approx F(A_\infty) - \left.\frac{dF}{dA}\right|_{A_\infty} \Delta A(t) = -\left.\frac{dF}{dA}\right|_{A_\infty} \Delta A(t), \qquad \textbf{[S5]}$$

where, by definition, $F(A_\infty) = dm/dt = 0$ at the steady-state. Using the chain rule, we can further write the rate of change for CheA activity in terms of the rate of change in methylation:

$$\frac{dA}{dt} = \frac{dA}{dm}\frac{dm}{dt} = -\frac{d\Delta A}{dt}. \qquad \textbf{[S6]}$$

Substituting Eq. **S5** into Eq. **S6**, we obtain

$$\frac{d\Delta A}{dt} \approx \frac{dA}{dm}\frac{dF}{dA}\bigg|_{A_\infty} \Delta A. \qquad \textbf{[S7]}$$

The first factor on the right-hand side of the equation represents how CheA activity is amplified by methylation; this factor is positive, and also proportional to N, the cluster size for interacting receptors. The second factor represents how the methylation rate depends on CheA activity at the steady-state; this factor is negative. These two factors combine to define the time constant with which CheA activity approaches its steady-state:

$$\frac{d\Delta A}{dt} \approx -\frac{N}{T}\Delta A, \qquad \textbf{[S8]}$$

where we have made the dependence on cluster size N explicit. Thus, CheA approaches its steady-state exponentially according to $\Delta A(t) = \Delta A_0 \exp(-Nt/T)$ (depicted in Fig. S9*A*).

Based on the above, we now use the Hill function, Eq. **S3**, to estimate the temporal response in bias $B(t)$, given $A(t)$ near the steady-state. For our purposes, we specifically determine the rate of change in $B(t)$ at the adaptation time; this will provide an approximate measure for the abruptness of the adaptation response (Fig. S9*A*), and its dependence on network parameters. Based on Eq. **S4** and **S8**, the rate of change in CheA activity at the adaptation time is

$$\frac{dA}{dt}\bigg|_{t_{\text{adapt}}} \approx \frac{N}{T}\Delta A(t_{\text{adapt}}) = \frac{N}{T}\frac{B_\infty}{2}\frac{dA}{dB}\bigg|_{B_\infty} \propto \frac{1}{H}\frac{N}{T}, \qquad \textbf{[S9]}$$

proportional to $1/H$. Using the chain rule, the rate of change in $B(t)$ at the adaptation time is then

$$\frac{dB}{dt}\bigg|_{t_{\text{adapt}}} = \frac{dB}{dA}\bigg|_{A(t_{\text{adapt}})}\frac{dA}{dt}\bigg|_{t_{\text{adapt}}} \propto H \cdot \frac{1}{H}\frac{N}{T} \propto \frac{N}{T}, \qquad \textbf{[S10]}$$

which is *independent* of H, given Eq. **S9** and the fact that the slope of the Hill function dB/dA at the adaptation time is proportional to H. Thus, the abruptness in the adaptation response for motor bias B does not depend on the sigmoidicity of the Hill function, Eq. **S3**, provided that H is sufficiently large. This is depicted schematically in Fig. S9*A*. While cooperativity amplifies the motor's response to changes in CheA activity (by a factor of H), it also makes the motor sensitive to small changes in CheA activity only near its steady-state. As CheA activity exponentially approaches steady-state during adaptation, its rate of change becomes smaller. Thus, the larger H is, the smaller the rate of change in CheA activity that engenders the motor response. These compensating effects result in a flagellar motor temporal adaptation response whose abruptness is largely independent of H (Fig. S9*A*). [Note that H does affect the adaptation time, but to a good approximation the shape of the response $B(t)$ remains unchanged.] Importantly, however, the dependence on cluster size N remains.

Possible role of dynamic receptor clustering in creating a stimulus-dependent adaptation abruptness. Clusters of chemotaxis receptors are known to be localized predominantly at the cell poles (42, 43), where the number of receptors in each cluster can range from tens to over 1,000 in the case of the Tar receptor (44). As mentioned above, experimental evidence indicates that receptors interact together to amplify their effect on CheA activity in response to external chemical inputs (29). The mathematical model (above) for the chemotaxis network (10, 32) further predicts that larger numbers of interacting receptors will result in a more abrupt response in CheA activity. Thus, abruptness in adaptation response likely originates from the clusters of interacting receptors that cooperatively modulate the activity of the kinase CheA. The abruptness at the level of CheA activity then propagates through the network to the level of whole-cell swimming behavior. Experimentally, CheA activity has only been measured in cell populations (13, 16, 45). We believe this may explain why abrupt adaptation kinetics in CheA has not yet been observed.

Experimental evidence also indicates that receptor clustering may be dynamic; when *E. coli* and *Bacillus subtilis* cells are stimulated with saturating amounts of attractant, the polar clusters disintegrate upon stimulation and reappear after the cells have had enough time to adapt (46, 47). In another study, Borrok et al. (48) found through chemical cross-linking studies that attractants destabilize receptor clusters and repellents stabilize them. These studies support a model in which the degree of chemoreceptor clustering changes dynamically depending on ligand binding. Given that the degree of receptor clustering decreases at higher attractant concentrations, it would be expected that their cooperative effect on CheA activity—and thus the abruptness in adaptation—would decrease. We note, however, that a number of studies found that receptor methylation level increases the degree of receptor clustering and hence the response cooperativity (30). Because methylation should increase with stimulus, this would predict that abruptness would decrease with stimulus, counter to the experimentally observed trend. We speculate that methylation level is low under our experimental conditions, and that this effect may be negligible. Unfortunately, experimental estimates of the methylation level exist only for mutant strains, lacking native receptors (30). Furthermore, theoretical estimates for the parameters that determine the steady-state methylation level vary greatly between different studies (10, 32). In our own simulations (which reproduce the experimental adaptation times), methylation saturates at about 2.5 out of the eight available sites at the highest stimulus level. It is also conceivable that the changes in receptor cluster size caused by methylation are small compared to those produced by ligand binding. More studies are needed to quantify the importance of these competing trends.

To investigate the possible role of receptor clusters, we performed simulations of chemotactic adaptation generalized to allow for strongly interacting receptor clusters of size N. Numerically solving the response to step up and step down in attractant concentration, we found that the simulated ETAs vary inversely with cluster size N (Fig. S10*B*). Specifically, the experimentally observed stimulus-dependent abruptness (Fig. 3*E*) can be reproduced by assuming that N varies between approximately 18 and 3, decreasing with stimulus strength (Fig. S10*C*). This range of values is consistent with numbers cited in the literature for wild-type (16, 30, 49) and mutant strains (30), and follows the expected trend with stimulus level. Thus, our simulations support the notion of dynamic receptor clustering as the source for adaptation abruptness and stimulus dependence. We also note that simulations corroborate our view that ETA is unaffected by the cooperativity H exhibited by CheY-P (Fig. S10*B*, *Inset*).

Possible role of motor remodeling in adaptation abruptness. Recent experiments (23) have uncovered another dynamic process during adaptation: flagellar motor remodeling. FliM, the component of the flagellar motor c-ring and the protein to which CheY-P binds to engender the conformational switch from CCW to CW rotation, is rapidly exchanged with free FliM in the cytosol. New evidence indicates that CheY-P binding increases the rate of dissociation of FliM from the c-ring, destabilizing it. As a result, changes in CheY-P levels in the cell during adaptation lead to changes in the flagellar motor structure. The net effect is that the dependence of the motor CW bias B on CheA activity A is dynamic. According to new models, the Hill function Eq. **S3** is modified to

$$B(A) = \frac{(1 + A/K_A)^{\mathrm{FliM}}}{(1 + A/K_A)^{\mathrm{FliM}} + P(1 + A/(K_A C))^{\mathrm{FliM}}}, \qquad \textbf{[S11]}$$

where P is the ratio of the probability that the motor is in the CCW state to the probability that it is in the CW state in the absence of CheY-P ($A = 0$), and C is the ratio of CheY-P dissociation constants for the CCW and CW states (23). The number of FliM proteins in the c-ring, FliM, is time-dependent, following

$$\frac{d}{dt}\mathrm{FliM} = V_{\mathrm{on}}(\mathrm{FliM}_{\mathrm{MAX}} - \mathrm{FliM}) - V_{\mathrm{off}}(A)\mathrm{FliM} \qquad \textbf{[S12]}$$

where V_{on} and V_{off} are the binding and (CheA-dependent) dissociation rates for FliM, and $\mathrm{FliM}_{\mathrm{MAX}}$ is the maximum number of FliM accommodated in the c-ring. The Hill function Eq. **S3** and the new model Eq. **S11** coincide with the following parameter values: $\mathrm{FliM} = 34$, $P = 10^7$ (50), and $C = 4.1$ (15, 51).

In principle, this recently discovered motor-remodeling mechanism can reproduce several features of adaptation kinetics that we observe at the whole-cell level. During the initial response to a step up in attractant, CheA activity drops, increasing the number of FliM in the flagellar motor. As shown schematically in Fig. S9*B* and observed directly in experiments (23), this increase in FliM shifts the sigmoidal CW bias vs. CheA activity curve (B vs. A) to the left. As a result, the steepest part of this curve no longer coincides with the steady-state CheA activity A_∞. Provided the shift persists as CheA activity A increases toward the steady-state, the time dependence of the CW bias $B(t)$ will be determined by $A(t)$ at a time point that precedes its slow, exponential approach to the steady-state A_∞, where its rate of change is far more rapid. This effect can lead to more-abrupt adaptation kinetics at the motor level (shown schematically in Fig. S9*B*). In addition, an overshoot response may be obtained if the remodeling shift persists at times long enough that A has approached its steady-state value. Whether these features are reproduced by FliM remodeling depends ultimately on how the time scales for motor remodeling compare to those for adaptation at the CheA level of the network.

We performed simulations incorporating flagellar motor remodeling (see *SI Materials and Methods*). As shown in Fig. S10*D*, we could reproduce an overshoot response for a reasonable choice of parameters.

1. Parkinson JS, Houts SE (1982) Isolation and behavior of *Escherichia coli* deletion mutants lacking chemotaxis functions. *J Bacteriol* 151:106–113.
2. Saini S, Brown JD, Aldridge PD, Rao CV (2008) FliZ Is a posttranslational activator of FlhD4C2-dependent flagellar gene expression. *J Bacteriol* 190:4979–4988.
3. Neuman KC, Chadd EH, Liou GF, Bergman K, Block SM (1999) Characterization of photodamage to *Escherichia coli* in optical traps. *Biophys J* 77:2856–2863.
4. Min TL, et al. (2009) High-resolution, long-term characterization of bacterial motility using optical tweezers. *Nat Methods* 6:831–835.
5. Alon U, Surette MG, Barkai N, Leibler S (1999) Robustness in bacterial chemotaxis. *Nature* 397:168–171.
6. Springer MS, Goy MF, Adler J (1979) Protein methylation in behavioural control mechanisms and in signal transduction. *Nature* 280:279–284.
7. Adler J, Templeton B (1967) The effect of environmental conditions on the motility of *Escherichia coli*. *J Gen Microbiol* 46:175–184.
8. Bustamante C, Chemla YR, Moffitt JR (2008) High resolution dual trap optical tweezers with differential detection. *Single-Molecule Techniques: A Laboratory Manual, eds* Selvin P, Ha TJ (Cold Spring Harbor Laboratory Press, Cold Spring Harbor, NY), pp vii, 507.
9. Gittes F, Schmidt CF (1998) Interference model for back-focal-plane displacement detection in optical tweezers. *Opt Lett* 23:7–9.
10. Tu Y, Shimizu TS, Berg HC (2008) Modeling the chemotactic response of *Escherichia coli* to time–varying stimuli. *Proc Natl Acad Sci USA* 105:14855–14860.
11. Park H, et al. (2010) Interdependence of behavioural variability and response to small stimuli in bacteria. *Nature* 468:819–823.
12. Lehmann EL, D'Abrera HJM (2006) *Nonparametrics: Statistical Methods Based on Ranks* (Springer, New York), revised 1st Ed, pp xvi, 463.
13. Meir Y, Jakovljevic V, Oleksiuk O, Sourjik V, Wingreen NS (2010) Precision and kinetics of adaptation in bacterial chemotaxis. *Biophys J* 99:2766–2774.
14. Vladimirov N, Lovdok L, Lebiedz D, Sourjik V (2008) Dependence of bacterial chemotaxis on gradient shape and adaptation rate. *PLoS Comput Biol* 4:e1000242.
15. Cluzel P, Surette M, Leibler S (2000) An ultrasensitive bacterial motor revealed by monitoring signaling proteins in single cells. *Science* 287:1652–1655.
16. Sourjik V, Berg HC (2002) Receptor sensitivity in bacterial chemotaxis. *Proc Natl Acad Sci USA* 99:123–127.
17. Alon U, et al. (1998) Response regulator output in bacterial chemotaxis. *EMBO J* 17:4238–4248.
18. Lovdok L, et al. (2009) Role of translational coupling in robustness of bacterial chemotaxis pathway. *PLoS Biol* 7:e1000171.
19. Elowitz MB, Levine AJ, Siggia ED, Swain PS (2002) Stochastic gene expression in a single cell. *Science* 297:1183–1186.
20. Li M, Hazelbauer GL (2004) Cellular stoichiometry of the components of the chemotaxis signaling complex. *J Bacteriol* 186:3687–3694.
21. Yu J, Xiao J, Ren X, Lao K, Xie XS (2006) Probing gene expression in live cells, one protein molecule at a time. *Science* 311:1600–1603.
22. Cai L, Friedman N, Xie XS (2006) Stochastic protein expression in individual cells at the single molecule level. *Nature* 440:358–362.
23. Yuan J, Branch RW, Hosu BG, Berg HC (2012) Adaptation at the output of the chemotaxis signalling pathway. *Nature* 484:233–236.
24. Korobkova EA, Emonet T, Park H, Cluzel P (2006) Hidden stochastic nature of a single bacterial motor. *Phys Rev Lett* 96:058105.
25. Endres RG, Wingreen NS (2006) Precise adaptation in bacterial chemotaxis through "assistance neighborhoods". *Proc Natl Acad Sci USA* 103:13040–13044.
26. Baker MD, Wolanin PM, Stock JB (2006) Signal transduction in bacterial chemotaxis. *Bioessays* 28:9–22.
27. Wadhams GH, Armitage JP (2004) Making sense of it all: Bacterial chemotaxis. *Nat Rev Mol Cell Biol* 5:1024–1037.
28. Liu JD, Parkinson JS (1989) Role of CheW protein in coupling membrane receptors to the intracellular signaling system of bacterial chemotaxis. *Proc Natl Acad Sci USA* 86:8703–8707.
29. Sourjik V, Berg HC (2004) Functional interactions between receptors in bacterial chemotaxis. *Nature* 428:437–441.
30. Endres RG, et al. (2008) Variable sizes of *Escherichia coli* chemoreceptor signaling teams. *Mol Syst Biol* 4:211.
31. Barkai N, Leibler S (1997) Robustness in simple biochemical networks. *Nature* 387:913–917.
32. Keymer JE, Endres RG, Skoge M, Meir Y, Wingreen NS (2006) Chemosensing in *Escherichia coli*: Two regimes of two-state receptors. *Proc Natl Acad Sci USA* 103:1786–1791.
33. Block SM, Segall JE, Berg HC (1983) Adaptation kinetics in bacterial chemotaxis. *J Bacteriol* 154:312–323.
34. Yi TM, Huang Y, Simon MI, Doyle J (2000) Robust perfect adaptation in bacterial chemotaxis through integral feedback control. *Proc Natl Acad Sci USA* 97:4649–4653.
35. Scharf BE, Fahrner KA, Turner L, Berg HC (1998) Control of direction of flagellar rotation in bacterial chemotaxis. *Proc Natl Acad Sci USA* 95:201–206.
36. Larsen SH, Reader RW, Kort EN, Tso WW, Adler J (1974) Change in direction of flagellar rotation is the basis of the chemotactic response in *Escherichia coli*. *Nature* 249:74–77.
37. Macnab RM, Han DP (1983) Asynchronous switching of flagellar motors on a single bacterial-cell. *Cell* 32:109–117.
38. Ishihara A, Segall JE, Block SM, Berg HC (1983) Coordination of flagella on filamentous cells of *Escherichia coli*. *J Bacteriol* 155:228–237.
39. Terasawa S, et al. (2011) Coordinated reversal of flagellar motors on a single *Escherichia coli* cell. *Biophys J* 100:2193–2200.
40. Turner L, Ryu WS, Berg HC (2000) Real-time imaging of fluorescent flagellar filaments. *J Bacteriol* 182:2793–2801.
41. Darnton NC, Turner L, Rojevsky S, Berg HC (2007) On torque and tumbling in swimming *Escherichia coli*. *J Bacteriol* 189:1756–1764.
42. Maddock JR, Shapiro L (1993) Polar location of the chemoreceptor complex in the *Escherichia coli* cell. *Science* 259:1717–1723.
43. Briegel A, et al. (2009) Universal architecture of bacterial chemoreceptor arrays. *Proc Natl Acad Sci USA* 106:17181–17186.
44. Greenfield D, et al. (2009) Self-organization of the *Escherichia coli* chemotaxis network imaged with super-resolution light microscopy. *PLoS Biol* 7:e1000137.
45. Shimizu TS, Tu Y, Berg HC (2010) A modular gradient-sensing network for chemotaxis in *Escherichia coli* revealed by responses to time-varying stimuli. *Mol Syst Biol* 6:382.
46. Lamanna AC, Ordal GW, Kiessling LL (2005) Large increases in attractant concentration disrupt the polar localization of bacterial chemoreceptors. *Mol Microbiol* 57:774–785.
47. Wu K, Walukiewicz HE, Glekas GD, Ordal GW, Rao CV (2011) Attractant binding induces distinct structural changes to the polar and lateral signaling clusters in *Bacillus subtilis* chemotaxis. *J Biol Chem* 286:2587–2595.
48. Borrok MJ, Kolonko EM, Kiessling LL (2008) Chemical probes of bacterial signal transduction reveal that repellents stabilize and attractants destabilize the chemoreceptor array. *ACS Chem Biol* 3:101–109.
49. Mello BA, Tu Y (2007) Effects of adaptation in maintaining high sensitivity over a wide range of backgrounds for *Escherichia coli* chemotaxis. *Biophys J* 92:2329–2337.
50. Stock J, Kersulis G, Koshland DE, Jr (1985) Neither methylating nor demethylating enzymes are required for bacterial chemotaxis. *Cell* 42:683–690.
51. Turner L, Caplan SR, Berg HC (1996) Temperature-induced switching of the bacterial flagellar motor. *Biophys J* 71:2227–2233.

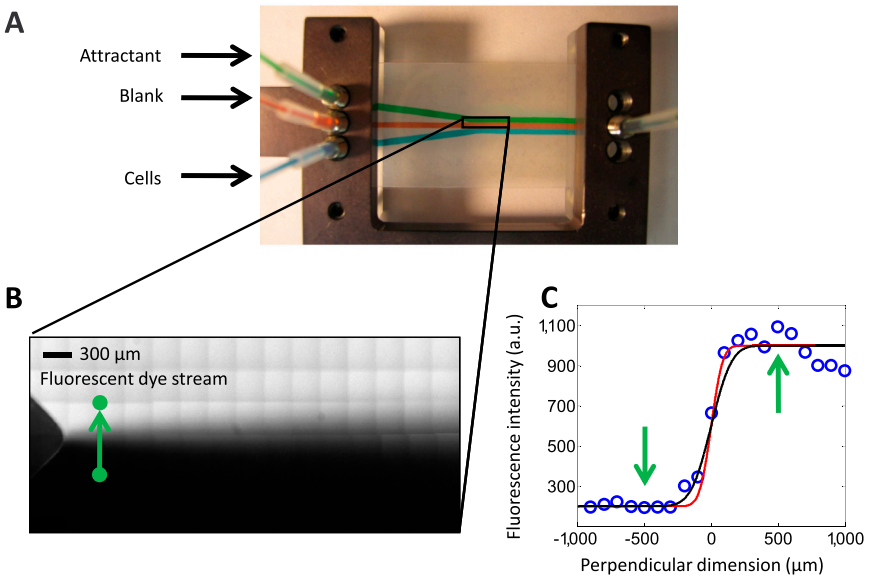

Fig. S1. Laminar flow chamber. (*A*) Photo of the laminar flow chamber used in this study. Food dyes of different colors were injected into different streams for illustration. (*B*) Fluorescence microscopy image of a typical gradient established in the flow chamber. The pixelated appearance of the image comes from the montage of multiple fields of view. Green dots indicate the pre- and poststimulus measurement locations, and the green arrow indicates the translocation direction of the trapped cell when stimuli are applied. (*C*) Concentration profile measured under the experimental conditions (linear flow speed = 70 μm/s, 500 μm downstream from where two streams merge). Fluorescence intensity of rhodamine B was measured at various points along the perpendicular direction (blue circles). Red and black smooth lines are theoretical concentration gradient curves with diffusion coefficient $D = 320\ \mu m^2/s$ (rhodamine B) and $D = 1000\ \mu m/s$ (small molecules), respectively. Green arrows indicate the pre- and poststimulus measurement locations. Theoretical concentrations at these locations are <1 and >99% of the maximum concentration at the low and the high ends, respectively. Taking the liberal estimation of $D = 1000\ \mu m^2/s$ for aspartate, cells that are moved along the concentration gradient at a speed of 100 μm/s experience the change from 10 to 90% of the maximum concentration over a span of about 3 s.

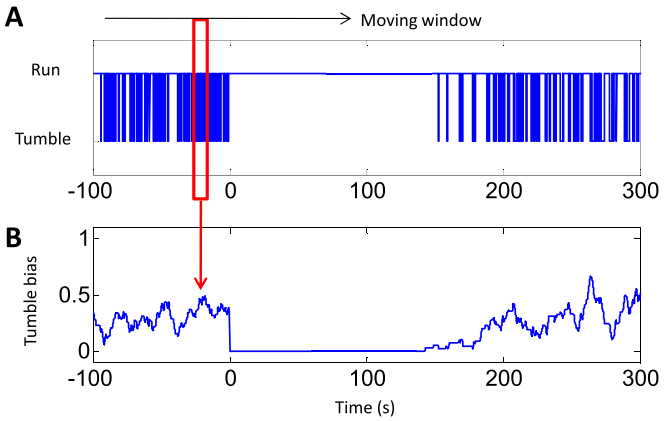

Fig. S2. Conversion from binary trace to tumble bias time trace. (*A*) A 400-s segment of a binary series from a single cell that underwent a 100-μM aspartate step-up stimulus at $t = 0$. (*B*) The tumble bias at each time point ($\Delta t = 0.01$ s) is determined from a 10-s moving window (red box) over the binary series.

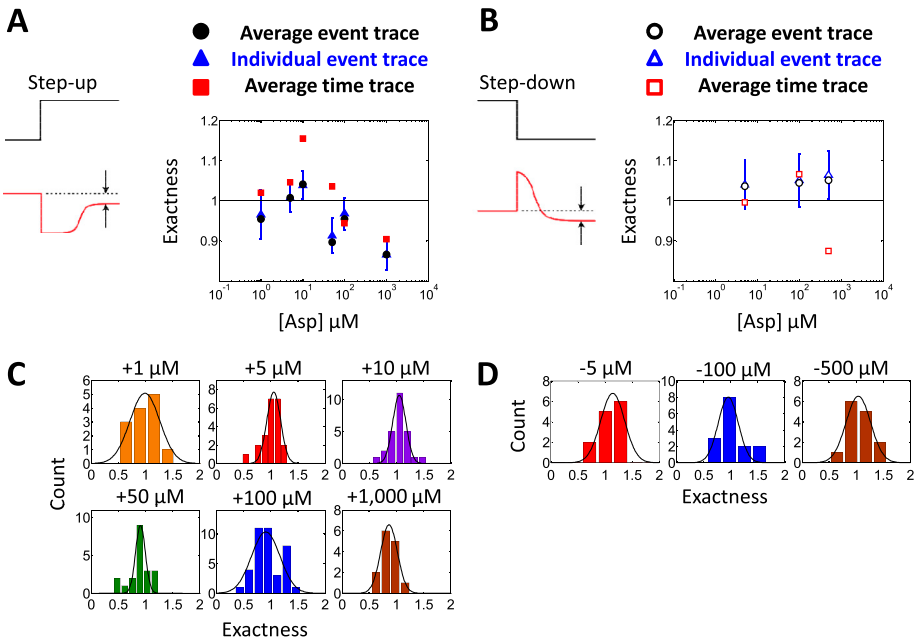

Fig. S3. Exactness of adaptation to step-up and step-down stimuli. (*A*) Exactness of adaptation determined from the individual cell event traces (blue triangles, mean ± standard error of the mean), population-average event traces (black circles), and population-average time traces (red squares). (*B*) Same as *A*, for step-down stimuli. (*C*) Histograms of single-cell adaptation exactness in response to varying magnitudes of step-up stimuli. (*D*) Same as *C*, for step-down stimuli. Black lines are fits to a Gaussian. Color notations and sample sizes at each stimulus level are the same as in Figs. 3 and 4. From event traces, exactness was defined as Bias_after/Bias_before, where Bias_after was the mean tumble bias of the final 20 events poststimulus, and Bias_before was the mean prestimulus tumble bias. From population-average time traces, exactness was define as the ratio of mean tumble bias of last 50 s after stimulus to mean tumble bias of 200 s before stimulus.

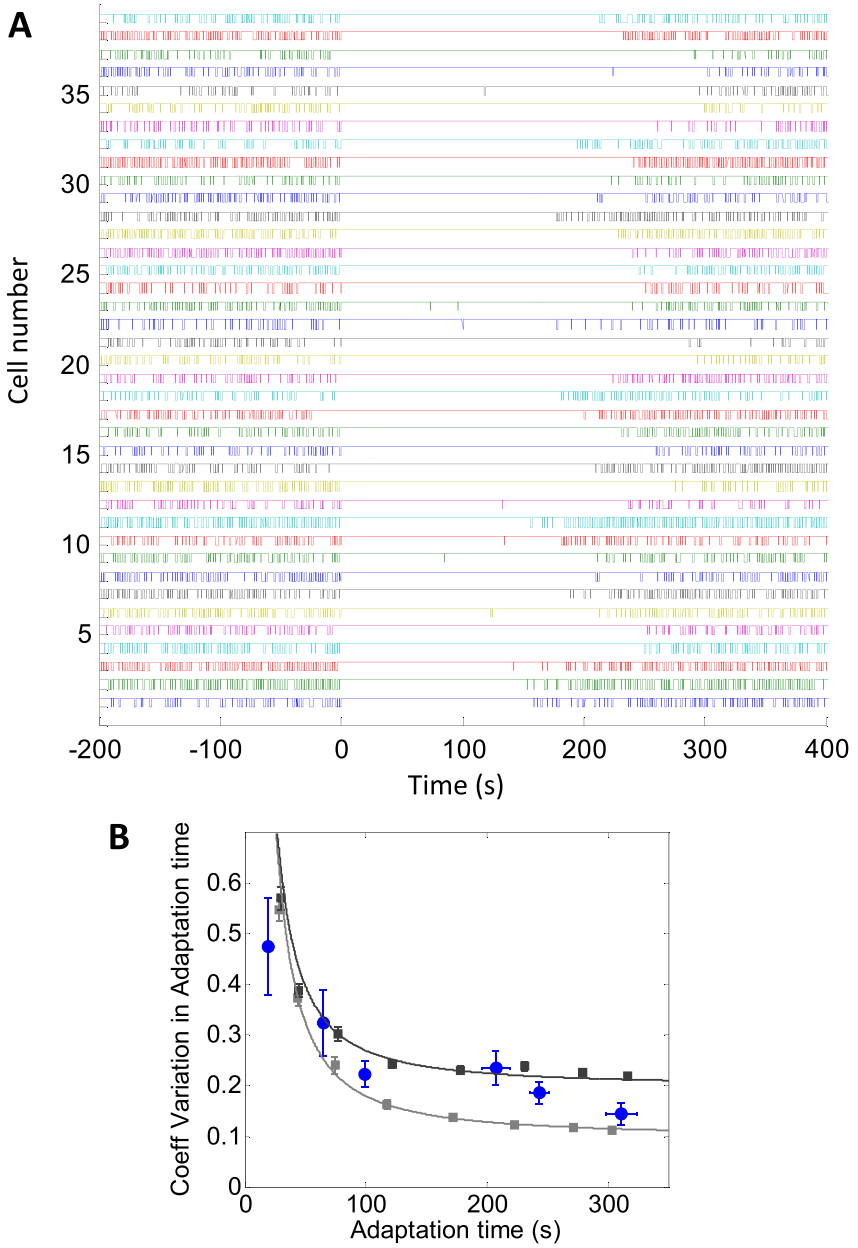

Fig. S4. Cell-to-cell variation in adaptation time. (*A*) Individual binary traces for 39 cells that underwent a 100-μM L-aspartate step-up stimulus (at $t = 0$). All cells initially respond to the stimulus by entering a prolonged run. The subsequent return to run/tumble switching occurred at different times for different cells. Individual cell traces are colored randomly. (*B*) The coefficient of variation (standard deviation divided by the mean) of adaptation time as a function of the average adaptation time. Blue circles, experimental data binned according to the applied stimulus strengths. Gray squares, numerical simulations of the chemotactic response at various stimulus strengths. For each stimulus strength, a population of 1,000 cells was simulated. Variation in adaptation times was obtained by selecting the methylation and demethylation rates by CheR and CheB for each cell from a Gaussian distribution with 10% (light gray squares) and 20% (dark gray squares) standard deviation. The ratio of methylation and demethylation rates was held constant. In all plots, error bars denote standard error, obtained by repeated resampling of the dataset (bootstrapping). Solid lines are guides to the eye. For details of the numerical simulations see *SI Materials and Methods*.

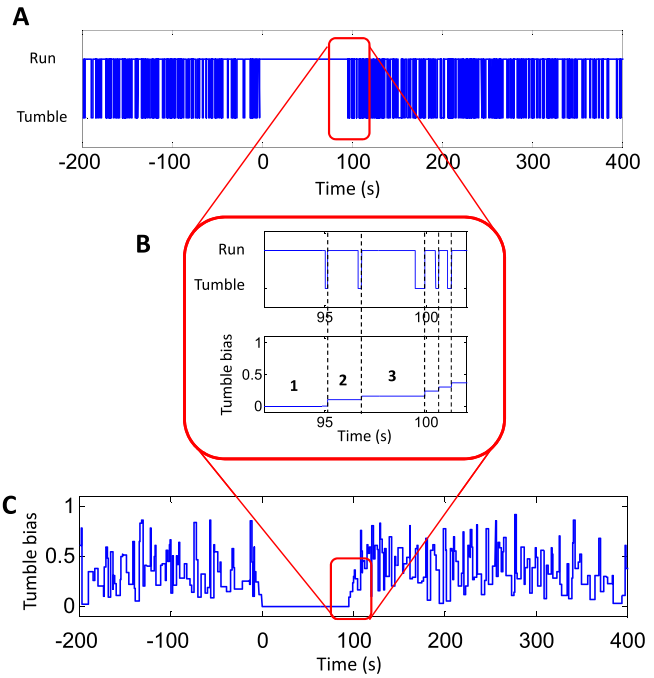

Fig. S5. Conversion from binary trace to tumble bias event trace. (*A*) A 600-s segment of a binary series from a single cell that underwent a 10-μM aspartate step-up stimulus at $t = 0$. (*B*) The tumble bias is calculated for each event pair consisting of a run and a tumble. Events are enumerated starting from the first event following the stimulus. (*C*) In addition to the tumble bias value, each event is aligned in time to the binary trace for visualization purposes.

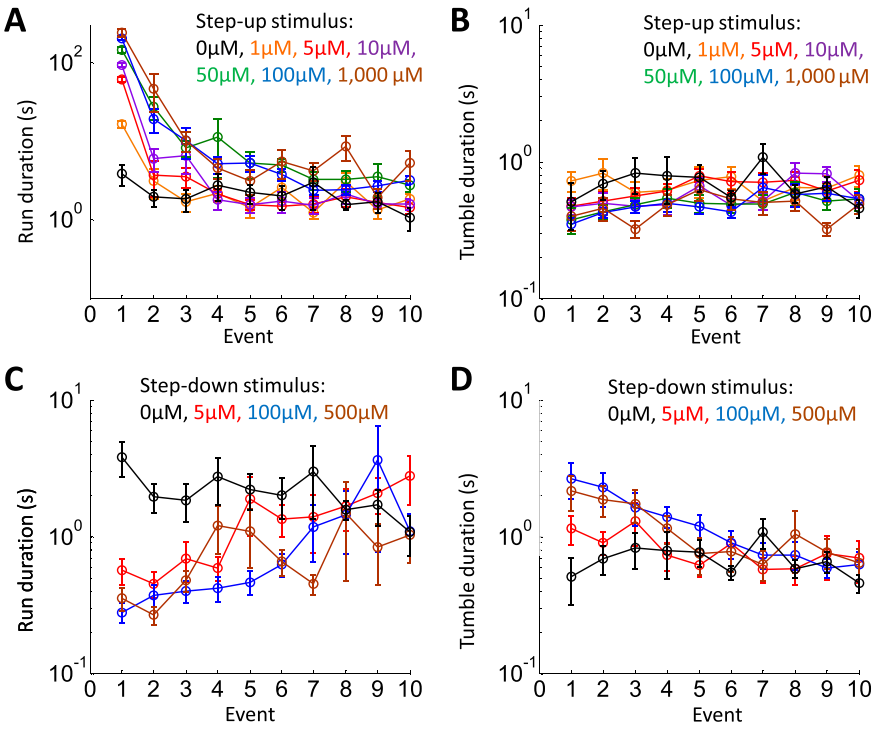

Fig. S6. Changes in average run and tumble durations following stimuli. (*A*) Population-averaged run durations of the first 10 events following step-up stimuli. Different stimulus strengths are color-coded as in the main figures. (*B*) Same as *A*, for tumble durations. (*C*) Same as *A*, for step-down stimuli. (*D*) Same as *B*, for step-down stimuli. Error bars designate standard error of the mean.

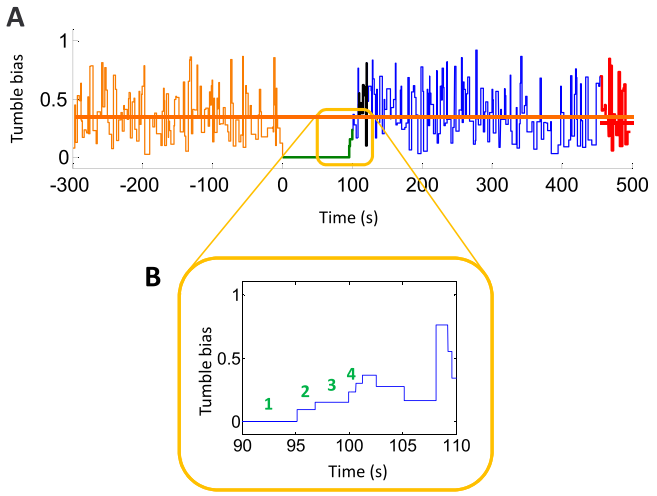

Fig. S7. Quantifying the adaptation parameters of an individual cell. (*A*) An 800-s segment of a tumble bias event trace from a single cell that underwent a 10-μM aspartate step-up stimulus at $t = 0$. Prestimulus events are in brown and poststimulus events are in blue. The four events that lead up to the cell's adaptation are highlighted in green (see *SI Materials and Methods* for determination of the number of events to adaptation). The 10 events following adaptation and the last 20 poststimulus events used to determine overshoot are highlighted in black and red, respectively (*SI Materials and Methods*). Exactness is determined from the mean tumble bias of the last 20 poststimulus events (red horizontal line), and the mean prestimulus tumble bias (brown horizontal line). (*B*) Zoomed-in view of the four events that lead up to adaptation.

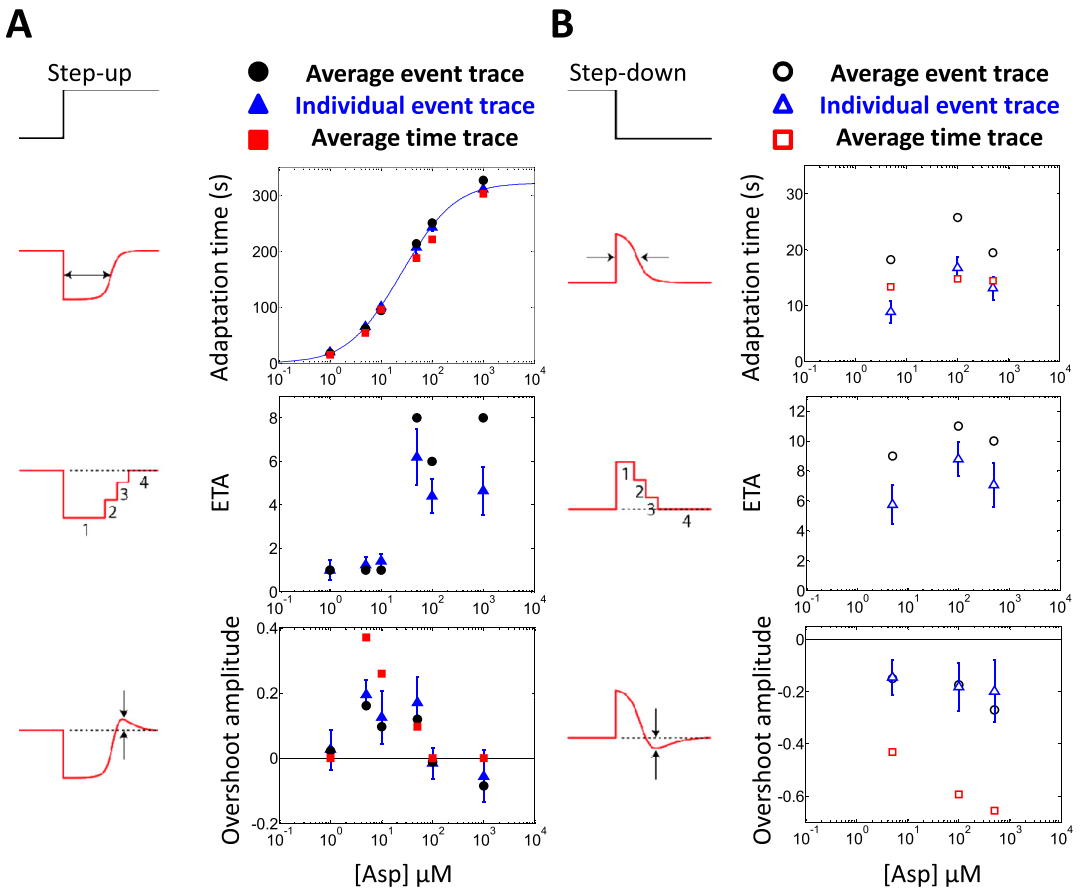

Fig. S8. Quantification of adaptation parameters at the single-cell and the population-average levels. (*A*) Adaptation parameters in response to step-up stimuli. From top to bottom, adaptation time, number of ETA, and normalized overshoot amplitude quantified from the individual cell event traces (blue triangles, mean ± standard error of the mean), population-average event traces (black circles), and population-average time traces (red squares). Schematics representing the step-up stimulus and each of the three behavioral parameters are shown on the left. ETA values were not obtained from population-average time traces. (*B*) Same as *A*, for step-down stimuli.

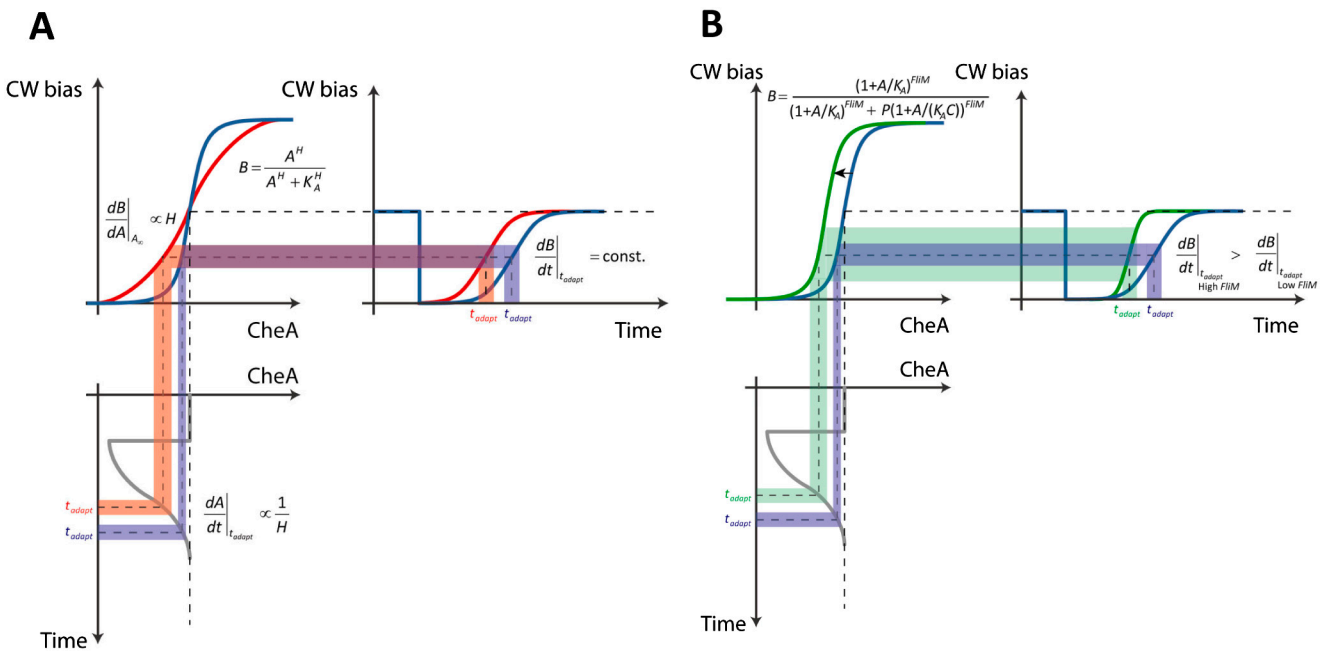

Fig. S9. Abruptness and its dependence on cooperative switching and FliM remodeling of the flagellar motors. (*A*) The effect of motor cooperativity. The schematic describes how the time course in CheA activity during adaptation, $A(t)$, (gray trace, *Bottom*; CheY-P level is proportional to CheA activity) is mapped into a corresponding motor bias time course, $B(t)$, (blue and red traces, *Right*) through the sigmoidal motor bias vs. CheA activity function $B(A)$ (red and blue traces, *Center*). Two different Hill functions are shown, with high Hill coefficient H (blue) and low H (red). At the adaptation time t_{adapt}, the high-H function amplifies changes in $A(t)$ near its steady-state, where its rate of change (represented by the shaded blue area) is small. Conversely, for the low-H function, the rate of change in $A(t)$ at t_{adapt} is larger (shaded red area), but amplified less. These compensating effects lead to a motor bias time course whose rate of change at t_{adapt} (its abruptness) is largely independent of H. See *SI Discussion* for more details. (*B*) The effect of FliM remodeling. The schematic describes how the time course in CheA activity during adaptation, $A(t)$, (gray trace, *Bottom*; CheY-P level is proportional to CheA activity) is mapped into a corresponding motor bias time course, $B(t)$, (blue and green traces, *Right*) through the sigmoidal motor bias vs. CheA activity function $B(A)$ (blue and green traces, *Center*). Two different motor curves are shown, which correspond to the flagellar motor in its steady-state configuration (blue) and remodeled configuration (green). The steady-state motor curve corresponds to the flagellar motor with equilibrium number of FliM units (low FliM), whereas the remodeled motor curve corresponds to the flagellar motor with transiently increased number of FliM units (high FliM). At the adaptation time t_{adapt}, the low-FliM curve amplifies changes in $A(t)$ near its steady-state where its rate of change (represented by the shaded blue area) is small. On the other hand, for the high-FliM curve, the rate of change in $A(t)$ at t_{adapt} is larger (shaded green area), and hence amplified more. As a result, the motor bias undergoes a more abrupt change in the case of the high-FliM curve. See *SI Discussion* for more details.

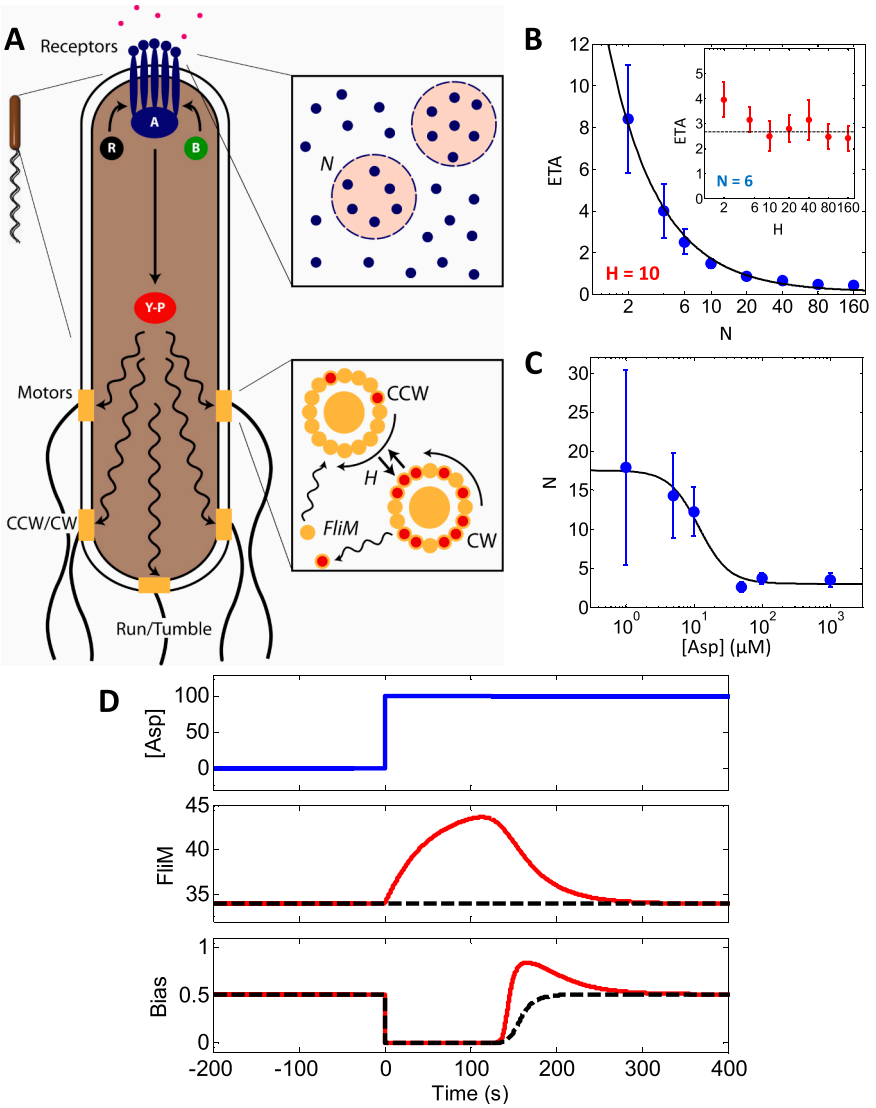

Fig. S10. Possible mechanisms giving rise to the observed adaptation abruptness and overshoot. (*A*) A schematic of the chemotaxis signaling network. Receptor clusters of size *N* modulate the CheA kinase activity in a cooperative manner, influenced by ligand binding and methylation/demethylation by CheR/CheB. CheA phosphorylates CheY into CheY-P, which then diffuses and binds the flagellar motors. The switching of the flagellar motors' rotational direction caused by the binding/unbinding of CheY-P to the FliM units on the motor occurs with cooperativity *H*. Binding of CheY-P to FliM, at the same time, lowers FliM's affinity to the rest of the flagellar motor. As a result, the number of FliM units on a motor increase over time in the absence of CheY-P. (*B*) The number of ETA as a function of the receptor cluster size *N*. Chemotactic response of individual cells to a 100-μM step up in L-aspartate concentration was simulated by numerically solving a stochastic model of the chemotaxis response, and the mean ETA was obtained by fitting exponential functions to the histogram of individual ETA values from 100 cells. Error bars denote the fitting uncertainty. The cooperativity of the flagellar motor switching behavior, *H*, was set at 10. Black line is a model fit in the form of $a/N + b$. (*Inset*) The effect of varying *H* on the ETA. The receptor cluster size, *N*, was set at six. (*C*) The estimated receptor cluster size *N* as a function of the step-up stimulus. *N* was estimated from the experimentally measured ETA (Fig. 3*E*), using the theoretical relation between ETA and *N* (as shown in *B*). Error bars designate the experimental standard error. (*D*) Numerical simulation of the effect of FliM remodeling on adaptation kinetics. (*Top*) A step-up stimulus of 100 μM L-aspartate was given $t = 0$. (*Middle*) With FliM remodeling incorporated into the simulation, the number of FliM units changes upon application of the stimulus (red solid line). The black dashed line shows the case of no FliM remodeling. (*Bottom*) Motor bias displays a more abrupt adaptation, and an overshoot, in the presence of FliM remodeling (red solid line) compared to the absence of FliM remodeling (black dashed line). For details of the numerical simulations see *SI Materials and Methods*.